Journal of Functional Materials and Applied Engineering

Research Paper

Air Oxygen activated and Efficient Oxidative Dehydrogenation of Terpinene Catalyzed by Multi metallic BiFeCo MOFs

Freya Olsen[1,*], Finn Berglund[1], Gustavo Silva[2]

[1] Department of Chemical Engineering, Massachusetts Institute of Technology, Cambridge, Massachusetts 02139, United States;
[2] School of Chemical & Biomolecular Engineering, Georgia Institute of Technology, Atlanta, Georgia 30332-0100, United States
*Corresponding author: Freya.Olsen@lancaster.ac.uk; Finn2014@lancaster.ac.uk; Gustavo.Silva@ornl.gov

Abstract. Heterometallic metal–organic frameworks bearing diverse metallic active sites show considerable promise for activating molecular oxygen catalytically, stemming from cooperative electronic interactions among distinct metal centres. Herein, a trimetallic MOF incorporating Bi^{3+}, Fe^{3+} and Co^{2+} nodes was fabricated through a static solvothermal approach and subsequently deployed for the aerobic oxidative dehydrogenation of terpinene with high efficiency. Comprehensive characterisation of the synthesised $Bi_2Fe_2Co_4$-MOF-BDC-150-24 catalyst—encompassing XRD, IR spectroscopy, SEM, XPS and NH_3-TPD—verified its robust architecture and the existence of electronic synergy among the multiple metal constituents. Operating under near-ambient conditions and in the absence of any external additives, the catalyst selectively transformed the C–C σ-bond in terpinene into a C=C π-bond, furnishing a conversion level of 96.1 %. Furthermore, the material displayed broad substrate scope, delivering 97.2 % conversion for γ-terpinene and 93.9 % for phellandrene. Durability assessments revealed that the catalyst retained its high activity over five successive cycles, attesting to outstanding recyclability and considerable practical potential.

Keywords: *Multi metallic BiFeCo MOFs; Air oxygen activation; Terpinene; Oxidative dehydrogenation; Synergistic catalyst*

Received on 02 April 2025, Accepted on 25 April 2025, Published on 11 June 2025

1 Introduction

Oxidative dehydrogenation (ODH) is an alternative to direct dehydrogenation of hydrocarbons for the production of high-value-added olefins in modern chemical industry[1-3]. The ODH process has significant thermodynamic advantages and lower energy consumption requirements, and has broad application prospects. It is an exothermic reaction and low temperature is favorable for the reaction[4]. Currently, the oxidants mainly used in the oxidative dehydrogenation process include oxygen[5-7], hydrogen peroxide[8-10], and organic peroxides[11,12], etc. Among them, hydrogen peroxide and organic peroxides (such as tert-butyl hydroperoxide) have problems such as high cost, low atom utilization, and difficulty in storage and transportation. As a cheap and easily accessible resource, oxygen only produces water after participating in oxidation reactions, so it can be used as a green oxidant for oxidative dehydrogenation reactions. However, the activation of oxygen molecules is relatively difficult, which leads to low utilization efficiency when used. Therefore, it is particularly urgent to develop catalytic materials that can efficiently activate molecular oxygen.

Metal–organic frameworks (MOFs) [13–15] are crystalline porous solids built from robust scaffolds, serving as sustainable catalysts for activating molecular oxygen. The periodic ordering of bridging ligands and metal nodes ensures homogeneous distribution of active centres, thereby enabling the full utilisation of every catalytic metal site. Therefore, MOFs materials have strong attractiveness in molecular oxygen activation[16,17]. Currently, reported MOFs materials with molecular oxygen activation performance mainly focus on single-metal materials. For example, Liu et al.[18] designed a special ligand containing benzothiadiazole units and used it to synthesize UiO-68 type MOF, which can efficiently activate molecular oxygen into superoxide radical anions ($O_2^{\cdot-}$) and singlet oxygen ($^1O_2$). Zwolinski and co-workers [19] covalently immobilised TEMPO radicals onto a Zr-MOF

scaffold to obtain a durable, highly active catalyst. Although this hybrid promoted the aerobic oxidative dehydrogenation of alcohols at room temperature, the system required t-Bu-ONO as an essential co-catalytic additive. Although single-metal MOF materials can activate molecular oxygen, they mainly rely on special organic ligands or cocatalysts. Sun et al.[20] reported a bimetallic ZrCo-MOF material. Compared with single-metal Co-MOF, it does not require the addition of other additives, and can efficiently activate molecular oxygen in air by utilizing the electronic synergy between Zr and Co. This implies that embedding diverse metal centres into the MOF scaffold modifies the local coordination environment, and that the resulting electronic synergy among these distinct metal sites equips the material with markedly improved catalytic capabilities. In this paper, Bi^{3+}[21] was used as the acid center, Fe^{3+}[22] and Co^{2+}[23,24] as oxidation centers, and a multi-metallic MOFs material BiFeCo-MOFs was designed and applied to the aerobic oxidative dehydrogenation of terpinene. Without adding other additives, $Bi_2Fe_2Co_4$-MOF-BDC-150-24 was used as a catalyst to achieve efficient conversion of terpinene under mild conditions, with a conversion rate of 96.1%. In addition, the catalyst showed high stability during recycling.

2 Experimental section

2.1 Synthesis of catalysts

Synthesis of Bi-MOF-BDC-150-24: Accurately weigh 3.881 g $Bi(NO_3)_3{\cdot}5H_2O$ (8.0 mmol) and dissolve it in 60 mL N,N-dimethylformamide (DMF). Then add 0.996 g terephthalic acid (H_2BDC, 6.0 mmol). Subsequently, place the polytetrafluoroethylene liner containing the solution on a magnetic stirrer, stir at room temperature for 4 h, then transfer it to a stainless-steel autoclave, and statically crystallize in an oven at 150 °C for 24 h. After that, take it out and cool to room temperature, wash 3 or 4 times with DMF and absolute ethanol, and dry overnight at 80 °C. The sample is denoted as Bi-MOF-BDC-150-24.

The synthesis process of Fe-MOF-BDC-150-24 is similar to that of Bi-MOF-BDC-150-24, except that $Fe(NO_3)_3{\cdot}9H_2O$ is used instead of $Bi(NO_3)_3{\cdot}5H_2O$. The synthesis process of Co-MOF-BDC-150-24 is similar to that of Bi-MOF-BDC-150-24, except that $Co(OAc)_2{\cdot}4H_2O$ is used instead of $Bi(NO_3)_3{\cdot}5H_2O$.

Synthesis of $Bi_2Fe_2Co_4$-MOF-BDC-150-24: Accurately weigh 0.970 g $Bi(NO_3)_3{\cdot}5H_2O$ (2.0 mmol), 0.808 g $Fe(NO_3)_3{\cdot}9H_2O$ (2.0 mmol) and 0.996 g $Co(OAc)_2{\cdot}4H_2O$ (4.0 mmol), dissolve them in 60 mL DMF, then add 0.996 g H_2BDC (6.0 mmol). Then place the polytetrafluoroethylene liner containing the solution on a magnetic stirrer, stir at room temperature for 4 h, then transfer it to a stainless-steel autoclave, and statically crystallize in an oven at 150 °C for 24 h. After that, take it out and cool to room temperature, wash 3 or 4 times with DMF and absolute ethanol, and dry overnight at 80 °C. The sample is denoted as $Bi_2Fe_2Co_4$-MOF-BDC-150-24.

The synthesis processes of other multi-metallic MOFs materials are similar to that of $Bi_2Fe_2Co_4$-MOF-BDC-150-24, but the parameters such as molar ratio of metal ions/ligand, Bi/Fe and (Bi+Fe)/Co molar ratios, synthesis temperature and time are different (Table S1, see Supporting Information of this paper).

2.2 Oxidative dehydrogenation reaction process

Into a 50 mL two-necked round-bottom flask were charged 50 mg of catalyst, 10.0 g cyclopentanone and 3.0 mmol terpinene. The flask was then immersed in a water bath held at 30 °C, and air was continuously sparged through the mixture at 30 mL min^{-1}. After 10 h of reaction, transfer part of the reaction solution to a centrifuge tube, centrifuge and analyze using a gas chromatograph (GC9720, FID flame ionization detector) to determine substrate conversion and product selectivity. The oxidation products of terpinene are shown in Scheme S1 (see Supporting Information of this paper), and the GC-MS characterization results of oxidation products are shown in Figure S1 (see Supporting Information of this paper).

3 Results and discussion

3.1 Characterization of catalysts

Figure 1(A) shows the XRD patterns of single-metal MOF and $Bi_2Fe_2Co_4$-MOF-BDC materials. From the figure, it can be seen that the Fe-MOF-BDC sample has diffraction peaks at 2θ = 12.6°, 17.6°, 25.4°, which is consistent with the report in literature[25], indicating that the Fe-MOF material was successfully prepared. The Bi-MOF-BDC sample has diffraction peaks at 2θ = 27.2°, 38.0°, 39.6°, 48.7°, 56.0°, which is consistent with the report in literature[26], indicating that this material was successfully prepared. The Co-MOF-BDC sample has diffraction peaks at 2θ = 8.9°, 14.1°, 15.7°, 17.8°, corresponding to the spectrum in literature[27], indicating that the material was successfully prepared. The $Bi_2Fe_2Co_4$-MOF-BDC sample has diffraction peaks at 2θ = 9.0°, 12.1°, 25.9°, 32.6°, 33.4°, 40.9°, 46.7°, 49.6°, 54.2°, 58.7°. Among them, the diffraction peak at 2θ = 9.0° corresponds to the Co-MOF-BDC sample, the diffraction peak at 2θ = 12.1° corresponds to the Fe-MOF-BDC sample, and the diffraction peak at 2θ = 25.9° corresponds to the Bi-MOF-BDC sample, indicating that the multi-metal MOF material was successfully prepared. Figure 1(B) presents the powder X-ray diffraction profiles of BiFeCo-MOF-BDC specimens prepared at varying metal-to-ligand stoichiometries. At low metal-ion/ligand ratios, the reflections are relatively weak, signalling poor crystalline order. As this ratio is progressively raised, the peaks associated with the Fe-MOF-BDC phase undergo a pronounced enhancement, whereas those corresponding to the Co-MOF-BDC and Bi-MOF-BDC domains show only modest gains. This trend indicates that increasing the metal-ion loading markedly facilitates the growth of crystalline Fe-BDC domains within the trimetallic framework.

Figure 1(C) presents the powder X-ray diffraction profiles of BiFeCo-MOF-BDC prepared at varying (Bi+Fe)/Co stoichiometries. At low ratios, reflections from Bi-BDC and Fe-BDC phases are weak, whereas the Co-BDC phase produces markedly stronger diffraction signals. As the overall metal content is raised, Bragg peaks corresponding to Bi-BDC and Fe-BDC domains progressively gain intensity, while those associated with the Co-BDC framework steadily diminish.

Figure 1(D) illustrates the XRD patterns of BiFeCo-MOF-BDC samples fabricated with different Bi/Fe molar ratios. When this ratio falls below 1:1, the material displays intense reflections for both Co-BDC and Fe-BDC phases alongside weak Bi-BDC signatures. Conversely, once the Bi/Fe ratio exceeds unity, the crystalline peaks of Co-BDC and Fe-BDC drop substantially, whereas the Bi-BDC intensity exhibits a modest upturn. This trend implies that excessive Bi^{3+} incorporation compromises the crystalline ordering of Co-BDC and Fe-BDC domains within the multimetallic framework.

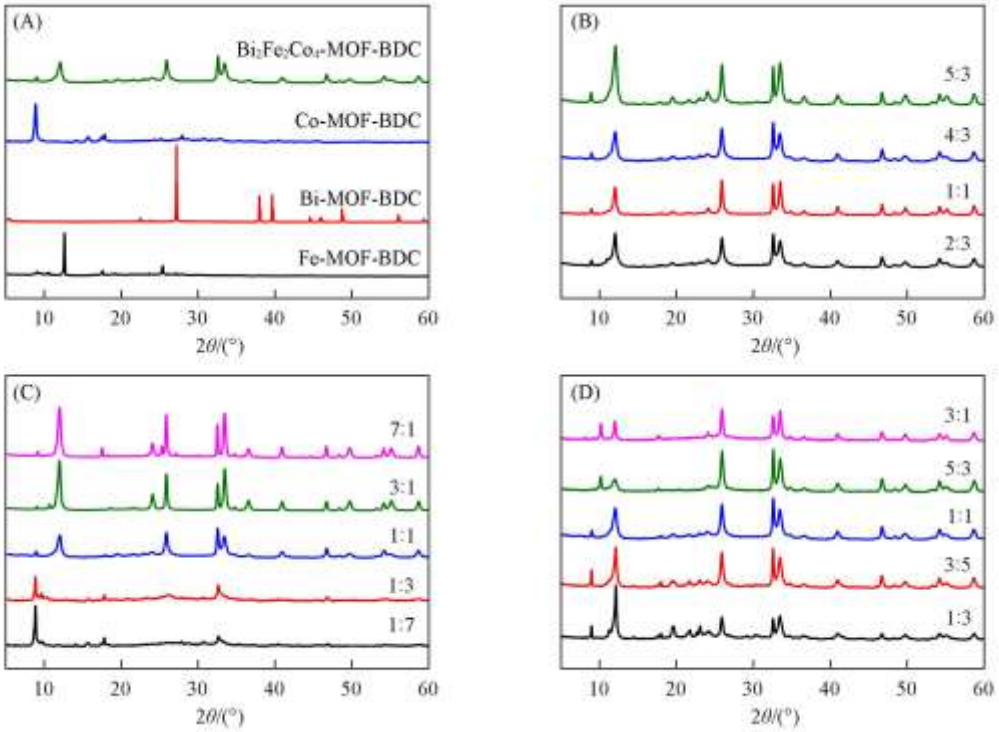

Figure 1 XRD patterns of BiFeCo▪MOFs material (a) Monometallic MOF and Bi2Fe2Co4-MOF-BDC; (b) different molar ratios of metal ions/ligands; (c) different molar ratios of (Bi+Fe)/Co; (d) different molar ratios of Bi/Fe.

Powder X-ray diffraction data presented in Figure S2(A) (Supporting Information) reveal how synthesis temperature influences the phase evolution of BiFeCo-MOF-BDC. Upon heating to 150 °C, the Co-BDC reflections remain essentially invariant, whereas the Bragg peaks associated with Fe-BDC and Bi-BDC domains progressively intensify. At elevated temperatures beyond this point, the Co-BDC and Fe-BDC signatures undergo a marked enhancement, while the Bi-BDC diffraction pattern shows negligible variation. Figure S2(B) (Supporting Information) displays the time-dependent crystallisation behaviour. During the early stages, the framework is still nucleating and growing, resulting in limited long-range order and hence weak overall scattering intensity. Prolonging the reaction duration causes the Fe-BDC and Bi-BDC peaks to steadily grow stronger, yet the Co-BDC profile remains largely unaffected. With further extension of time, the diffraction peak intensities of Fe-BDC and Bi-BDC structures in the material further increase, while the diffraction peak intensity of Co-BDC structure relatively decreases.

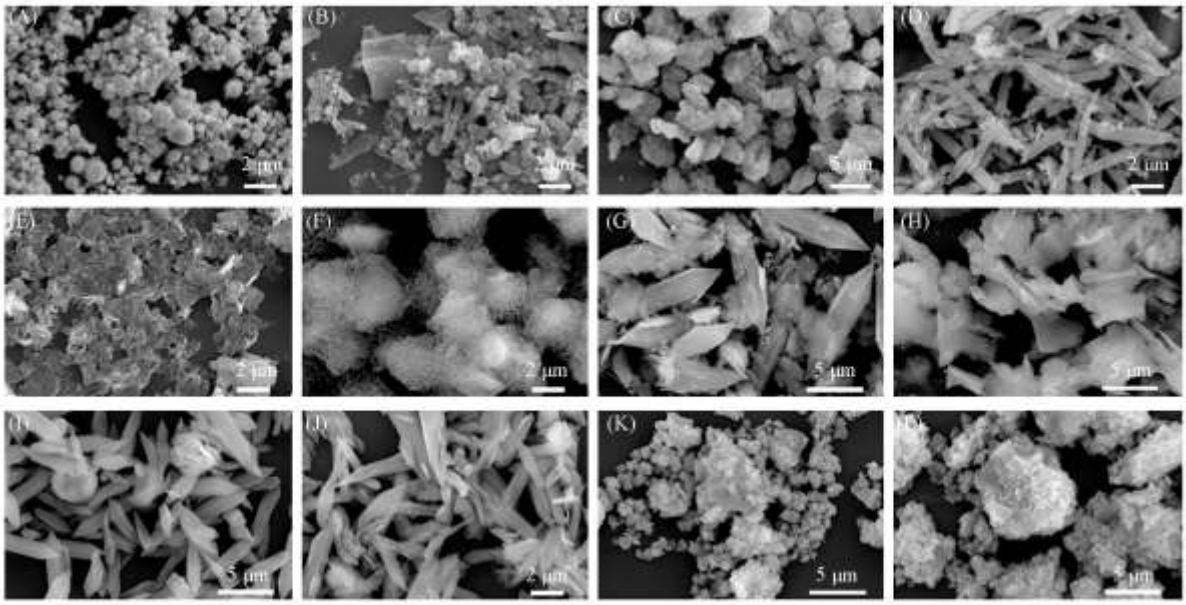

Figure 2 SEM images of different MOFs (a) Bi-MOF-BDC; (b)Fe-MOF-BDC; (c) Co-MOF-BDC; different molar ratios of (Bi+Fe)/Co: (d) 1:1, (e) 1:7, (f) 1:3, (g) 3:1; different molar ratios of Bi/Fe: (h) 1:1, (i) 1:3, (j) 3:5, (k) 5:3, (l) 3:1.

Thermogravimetric analysis (TGA) was employed to evaluate the thermal robustness of the as-synthesised MOF architectures. The corresponding thermograms and quantitative mass-loss data across defined temperature windows for the monometallic frameworks alongside the trimetallic $Bi_2Fe_2Co_4$-MOF-BDC are compiled in Figure S3 and Table S2 (Supporting Information). In the initial 30–250 °C interval, mass loss is predominantly ascribed to the expulsion of physisorbed water, with recorded losses of 2.3 %, 8.7 %, 8.0 % and 9.4 % for Bi-MOF-BDC, Fe-MOF-BDC, Co-MOF-BDC and $Bi_2Fe_2Co_4$-MOF-BDC, respectively. Between 250 °C and 485 °C, the observed weight reduction reflects the liberation of coordinated water molecules together with the thermal decomposition of unbound carboxylic functionalities, registering losses of 6.4 %, 51.8 %, 36.4 % and 27.4 %, respectively. Finally, in the elevated 485–800 °C domain, catastrophic framework decomposition and structural disintegration account for the high-temperature mass decline. Among them, Co-MOF-BDC has the highest weight loss rate (22.6%), while Fe-MOF-BDC and $Bi_2Fe_2Co_4$-MOF-BDC have weight loss rates of 12.3% and 13.1%, respectively. Bi-MOF-BDC has a weight loss rate of only 2.5%, with a total weight loss of 11.2%, showing the best thermal stability. Collectively, these data demonstrate that bismuth incorporation markedly bolsters the thermal resilience of the heterometallic MOF framework. Nitrogen-sorption analysis was performed on both the monometallic congeners and the $Bi_2Fe_2Co_4$-MOF-BDC sample; the resulting isotherms and pore-size distributions are presented in Figure S4 and Table S3 (Supporting Information). BET surface areas for all

frameworks lie between 10 and 25 $m^2 g^{-1}$, signalling virtually absent internal porosity. The limited surface area most likely arises from external crystal imperfections and inter-particulate voids rather than from intrinsic microporous channels. The pore volume of the $Bi_2Fe_2Co_4$-MOF-BDC sample is significantly increased compared with Bi-MOF-BDC and Fe-MOF-BDC materials, and is close to that of Co-MOF-BDC material. Compared with single-metal MOF materials, the average pore size of $Bi_2Fe_2Co_4$-MOF-BDC material increases, which may be due to the generation of more defect sites during crystal growth when different metal ions jointly construct the skeleton structure of the MOF material. The increase in pore volume and average pore size may be beneficial to the adsorption of molecular oxygen and substrate molecules on the surface of $Bi_2Fe_2Co_4$-MOF-BDC material, and have a certain promotion effect on the activation of molecular oxygen and the mass transfer process of reactant molecules.

Figure 2 shows the SEM images of single-metal MOF and $Bi_2Fe_2Co_4$-MOF-BDC materials. Bi-MOF-BDC is irregular spherical crystals [Figure 2(A)], Fe-MOF-BDC is irregular flake-like [Figure 2(B)], Co-MOF-BDC is irregular block-like [Figure 2(C)], while $Bi_2Fe_2Co_4$-MOF-BDC is slender shuttle-shaped crystals [Figure 2(D)], and the morphology is obviously different from single-metal materials, indicating the successful synthesis of multi-metal MOF. EDX analysis (Figure 3) further confirmed that C, O, Bi, Fe and Co elements are uniformly distributed in the material [Figure 3(A)], and the energy spectrum [Figure 3(B)] also shows the characteristic peaks of each element, confirming its successful synthesis and uniform distribution of elements. Figure 2 also shows the morphology evolution of BiFeCo-MOF-BDC under different (Bi+Fe)/Co molar ratios: at low molar ratio, it is irregular flake-like [Figure 2(E)]; with the increase of molar ratio, small-sized needle-like crystals appear [Figure 2(F)]; at a molar ratio of 1:1, larger shuttle-shaped crystals are formed [Figure 2(D)]; when the molar ratio continues to increase, the size of shuttle-shaped crystals increases [Figure 2(G)]; when the molar ratio is too high, it turns into large-sized irregular block structures [Figure 2(H)], indicating that too high Bi and Fe content is not conducive to morphology regularity. The effect of different Bi/Fe molar ratios on morphology is shown in Figures 2(I)-(L). At a molar ratio of 1:3, the crystals are shuttle-shaped with different sizes [Figure 2(I)]; when the molar ratio increases to 3:5, the size decreases [Figure 2(J)]; at 1:1, more uniform-sized shuttle-shaped crystals are formed [Figure 2(D)]; when the molar ratio is further increased, small-sized irregular blocks appear [Figure 2(K)]; at a molar ratio of 3:1, the block-shaped crystals increase significantly [Figure 2(L)].

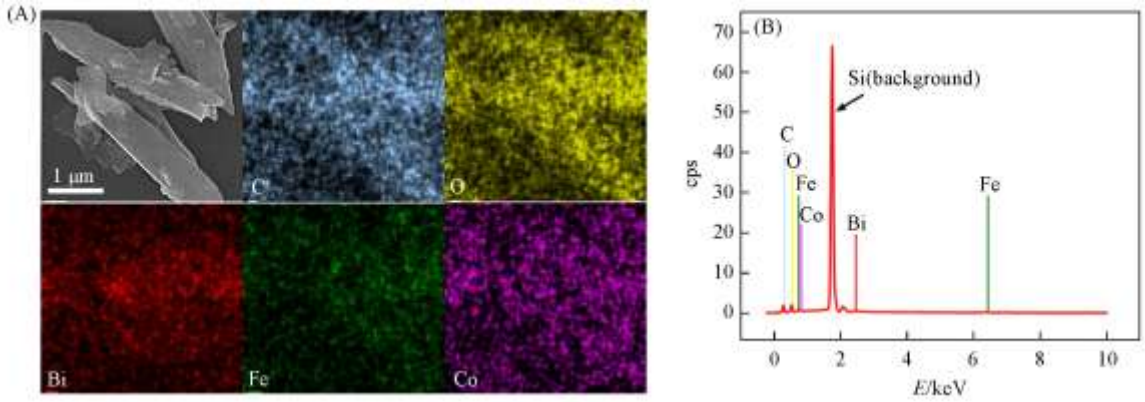

Figure 3 Element mapping(A) and EDX spectrum(B) of Bi2Fe2Co4-MOF-BDC-150-24

Figure S5 (see Supporting Information of this paper) shows SEM images of BiFeCo-MOF-BDC synthesized with different molar ratios of metal ions/ligands. When the molar ratio is 2:3 [Figure S5(A)], the material shows a mixed morphology of small-sized needle-like crystals and shuttle-shaped crystals of different sizes; when the molar ratio increases to 1:1 [Figure S5(B)], needle-like crystals decrease, shuttle-shaped crystals increase but sizes are uneven; at a molar ratio of 4:3 [Figure S5(C)], the crystals are mainly regular shuttle-shaped structures with similar sizes; further increasing the molar ratio [Figure S5(D)] leads to the enlargement of shuttle-shaped crystals and connection into block aggregates, indicating that too high metal ion content is not conducive to the formation of regular shuttle-shaped crystals. Figure S6 (see Supporting Information of this paper) shows SEM images of materials synthesized at different temperatures. At 110 °C [Figure S6(A)], the crystals are mainly irregular blocks, with few shuttle shapes, indicating slow crystallization at low temperature; at 130 °C [Figure S6(B)], shuttle-shaped crystals begin to appear, but still contain block crystals; at 150 °C [Figure S6(C)], most

crystals are uniform slender shuttle shapes; when the temperature is further increased [Figure S6(D)], the size distribution of shuttle-shaped crystals becomes wider, indicating that too high temperature leads to decreased crystallization controllability. Figure S7 (see Supporting Information of this paper) shows the effect of synthesis time on material morphology. After 12 h of reaction [Figure S7(A)], the size difference of shuttle-shaped crystals is significant; extending the reaction to 18 h [Figure S7(B)], the size difference decreases; after 24 h of reaction [Figure S7(C)], the crystal morphology is uniform and regular; continuing the reaction to 36 h [Figure S7(D)], the crystal size increases and stacking occurs, and irregular block structures appear in some areas.

XPS was used to analyze the chemical states of elements in Bi-MOF-BDC, Fe-MOF-BDC, Co-MOF-BDC and $Bi_2Fe_2Co_4$-MOF-BDC (Figure 4). In the survey spectrum of Figure 4(A), characteristic peaks of Bi_{4f}, Fe_{2p} and Co_{2p} can be seen, proving that Bi, Fe and Co coexist in the multi-metal MOF skeleton. High-resolution spectra [Figure 4(B)] show that the binding energy of $Bi_{4f7/2}$ in $Bi_2Fe_2Co_4$-MOF-BDC (159.6 eV) is 0.2 eV higher than that in Bi-MOF-BDC (159.4 eV); the binding energy of $Fe_{2p3/2}$ (711.6 eV) is 0.2 eV lower than that in Fe-MOF-BDC (711.8 eV) [Figure 4(C)]; the binding energy of $Co_{2p3/2}$ (781.3 eV) is 0.3 eV higher than that in Co-MOF-BDC (781.0 eV) [Figure 4(D)]. These binding energy shifts indicate that the introduction of Fe^{3+} causes electron cloud shifts of Bi^{3+} and Co^{2+}. Specifically, the upshift in Co^{2+} binding energy promotes the capture and activation of dioxygen molecules while facilitating singlet-oxygen generation; meanwhile, the increased Bi binding energy strengthens its electron-withdrawing character, thereby accelerating substrate adsorption and activation.

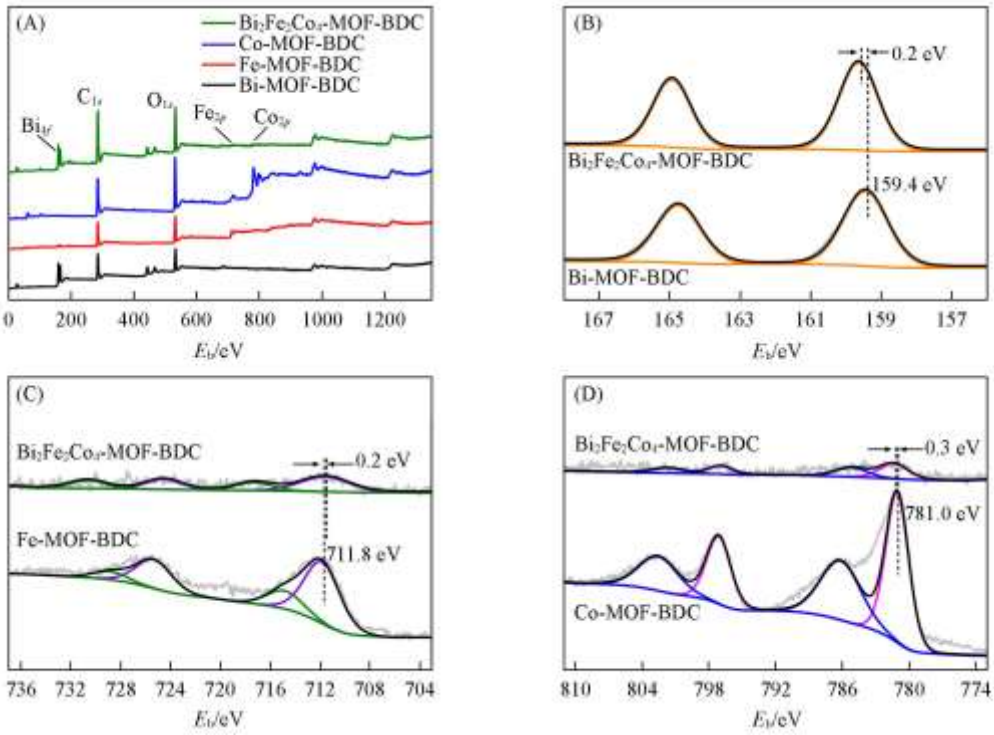

Figure 4 XPS spectra of monometallic MOF and Bi2Fe2Co4▪MOF▪BDC (a) Survey spectra; (b) Bi4f; (c) Fe2p; (d) Co2p.

NH_3-TPD was used to systematically study the acidity of different MOF materials. As shown in Figure 5(A), Co-MOF-BDC only has a weak desorption peak near 220 °C, with a total acid amount of 0.531 mmol/g, indicating that it only contains a small number of weak acid sites. The desorption peak of Fe-MOF-BDC is located near 250 °C, with a total acid amount of 2.837 mmol/g, and both acid site strength and quantity are improved. The total acid amount of Bi-MOF-BDC is slightly lower (2.213 mmol/g), but its desorption peak is located at about 440 °C, showing significantly higher acid strength. The total acid amount of multi-metal $Bi_2Fe_2Co_4$-MOF-BDC reaches 5.138 mmol/g, and the desorption peak is also located at about 440 °C, indicating that the synergistic effect of multiple metal ions successfully constructs abundant and strong acid sites, which is beneficial to catalytic reactions. Figure 5(B) shows that with the increase of (Bi+Fe)/Co molar ratio, the total acid amount of

BiFeCo-MOF-BDC first increases and then decreases. At low ratios, the insufficient content of Bi^{3+} and Fe^{3+} leads to limited formation of strong acid sites. Appropriately increasing the ratio can enhance acidity, but too high a molar ratio instead leads to a decrease in acid amount. Combined with XRD and SEM analysis, it can be seen that although too high a molar ratio can improve crystallinity and construct more acid sites, the large crystal size will bury the sites, reducing the apparent acidity. Figure 5(C) shows that with the increase of Bi/Fe molar ratio, the total acid amount gradually increases. XRD results show that with the increase of Bi/Fe molar ratio, the diffraction peak intensity of Fe-BDC structure weakens, and the diffraction peak intensity of Bi-BDC structure first increases and then slightly decreases, indicating that acid sites are mainly built around Bi^{3+} centers, so the increase in Bi^{3+} molar ratio directly enhances the acidity of the material.

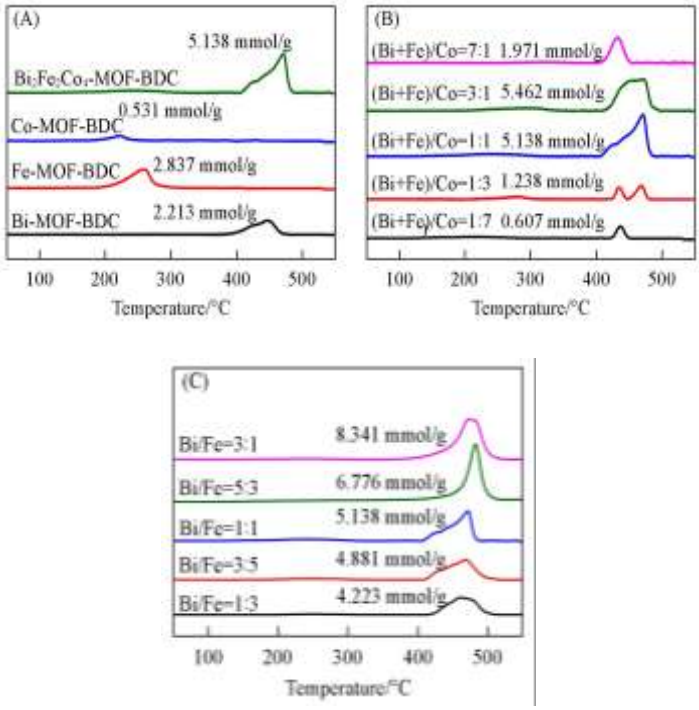

Figure 5 NH3-TPD curves of different MOFs (a) Monometallic MOF and Bi2Fe2Co4-MOF-BDC; (b) different molar ratios of (Bi+Fe)/Co; (c) different molar ratios of Bi/Fe.

3.2 Selective oxidative dehydrogenation of terpinene

Table 1 summarizes the reaction results of terpinene oxidative dehydrogenation catalyzed by different MOF materials. Without catalyst, the reaction hardly occurs (Entry 1). When Bi-MOF-BDC or Fe-MOF-BDC is used, there is also no activity (Entries 2, 3). Co-MOF-BDC has low catalytic activity, with a conversion of only 52.8% (Entry 4). The conversions of Bi_2Co_4-MOF-BDC and Fe_2Co_4-MOF-BDC increase to 70.0% and 75.9%, respectively (Entries 6, 7), indicating that their activities are slightly better than that of Co-MOF-BDC. When the multi-metal $Bi_2Fe_2Co_4$-MOF-BDC with Bi^{3+}, Fe^{3+} and Co^{2+} as co-metal centers is used (Entry 8), the conversion reaches 96.1%, which is significantly higher than the catalytic effect of the physical mixture of three single-metal MOFs (Entry 5), indicating that the three metals coexist in the skeleton in a coordination form rather than simple physical mixing. Combined with XPS analysis, Fe^{3+} causes Co^{2+} electron cloud shift, promoting its conversion to Co^{3+}, thereby enabling the adsorbed oxygen molecules to obtain electrons and be activated into singlet oxygen species. At the same time, the introduction of Bi^{3+} provides abundant strong Lewis acid sites, which is beneficial to substrate adsorption and promotes C-H bond cleavage. Therefore, the synergistic effect of Fe^{3+} and Co^{2+} in multi-metal MOF effectively improves oxygen activation efficiency, and the strong acidity provided by Bi^{3+} jointly endows the material with excellent catalytic performance.

Figure 6(A) illustrates how the metal-to-ligand stoichiometry influences the catalytic performance of BiFeCo-MOF-BDC. Terpinene conversion rises progressively as the molar ratio increases, whereas p-cymene selectivity

peaks at a 4:3 metal-ion/ligand ratio after an initial ascent followed by a decline. XRD and SEM analyses reveal that low metal-to-ligand ratios yield poorly crystallised products exhibiting a heterogeneous morphology comprising fine needle-like crystallites alongside variably sized shuttle-shaped particles. Under these conditions, the scarcity of accessible active sites accounts for the diminished catalytic activity. As the amount of metal ions increases, the material gradually grows into a regular shuttle-shaped crystal structure, and the number of catalytic active sites constructed in the material gradually increases, enhancing the catalytic activity of the material. Further growth of crystals indicates that more catalytic active sites are constructed, but too many acid sites will lead to increased side reactions, resulting in a decrease in product selectivity. Therefore, the optimal molar ratio of metal ions/ligands is 4:3.

Table 1 Oxidative dehydrogenation of terpinene over different materials

Entry	Catalyst	Conversion(%)	Selectivity(%)
1	—	—	—
2	Bi-MOF-BDC-150-24	2.5	100
3	Fe-MOF-BDC-150-24	1.6	100
4	Co-MOF-BDC-150-24	52.8	77.9
5	Bi-MOF/Fe-MOF/Co-MOF (physical mixture)	42.7	78.3
6	Bi_2Co_4-MOF-BDC-150-24	70.0	73.6
7	Fe_2Co_4-MOF-BDC-150-24	75.9	75.3
8	$Bi_2Fe_2Co_4$-MOF-BDC-150-24	96.1	88.5

*Reaction conditions: 50 mg catalyst, 3 mmol terpinene, 10 g cyclopentanone, 30 °C, 10 h, air flowrate: 30 mL/min.

Figure 6(B) shows the effect of (Bi+Fe)/Co molar ratio on the catalytic activity of BiFeCo-MOF-BDC material. From the figure, it can be seen that with the increase of (Bi+Fe)/Co molar ratio, the conversion of terpinene and the selectivity to p-cymene both first increase and then decrease. Combined with relevant characterization, it can be explained that when the (Bi+Fe)/Co molar ratio is low, due to the low content of Bi^{3+} and Fe^{3+} in the material, the interaction between Fe^{3+} and Co^{2+} is weak, so the air oxygen activation efficiency is low, leading to slow substrate conversion. At the same time, SEM characterization shows that when the molar ratio is lower than 1:1, the material cannot form a regular shuttle-shaped morphology. Although flake and needle structures are beneficial for catalyst contact with substrate molecules, NH_3-TPD analysis results show that the number of strong acid sites provided by Bi^{3+} in the material is low, resulting in weak interaction with the C=C double bond in substrate molecules, leading to low substrate activation efficiency and low selectivity to p-cymene. When the (Bi+Fe)/Co molar ratio is increased, although the decrease in Co^{2+} content in the material reduces the molecular oxygen activation efficiency, the acidity of the material is significantly enhanced, which makes substrate activation easier, thereby enabling terpinene to be rapidly converted to p-cymene with high selectivity. However, when the (Bi+Fe)/Co molar ratio is too high, the Co^{2+} content in the BiFeCo-MOF-BDC material decreases significantly, and the material grows into large-sized irregular block structures, leading to a reduction in catalytic active sites exposed on the crystal surface, reducing the efficiency of the material to activate molecular oxygen, thereby significantly reducing the catalytic activity, and the weakening of material acidity also leads to a decrease in product selectivity. Therefore, the optimal (Bi+Fe)/Co molar ratio is 1:1. Figure 6(C) shows the effect of Bi/Fe molar ratio on the catalytic activity of BiFeCo-MOF-BDC. From the figure, it can be seen that when the molar ratio is 1:3 or 3:5, both substrate conversion and product selectivity are low, which is significantly related to the low acid strength of the material. As the amount of Bi^{3+} introduced increases, the acidity of the material gradually increases, and the shuttle-shaped crystals gradually grow into a regular and uniform shape. The active sites on the crystal surface can be well exposed, increasing the efficiency of catalyst adsorption and activation of substrates, so the catalytic activity of the material also gradually increases. When the Bi/Fe molar ratio exceeds 1:1, the conversion of terpinene and the selectivity to p-cymene significantly decrease. The characterization results of the material show that excessive introduction of Bi^{3+} will cause a certain degree of decrease in the crystallinity of the material, and the morphology of the material also changes from shuttle-shaped to irregular

block structures, so that the fewer metal active sites formed in the material cannot be well exposed, leading to a decrease in air oxygen activation efficiency. The further increase in acid strength of the material leads to a decrease in selectivity, indicating that too strong acidity is not conducive to the formation of p-cymene. Based on the above results, the most suitable Bi/Fe molar ratio is determined to be 1:1.

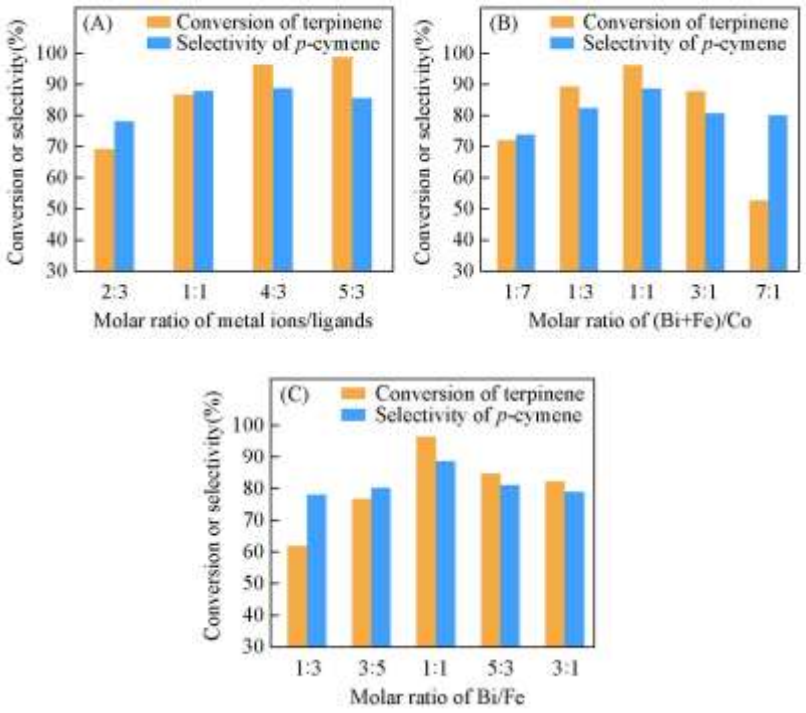

Figure 6 Effect of synthesis conditions on the catalytic activity of BiFeCo▪MOF▪BDC (a) Molar ratios of metal ions/ligands; (b) molar ratios of (Bi+Fe)/Co; (c) molar ratios of Bi/Fe. Reaction conditions: 50 mg catalyst, 3 mmol terpinene, 10 g cyclopentanone, 30 ℃, 10 h, air flowrate： 30 mL/min.

Figure S8(A) (see Supporting Information of this paper) shows that the effect of synthesis temperature on the catalytic performance of BiFeCo-MOF-BDC first increases and then decreases, and at 150 °C, both terpinene conversion and p-cymene selectivity reach the highest. At low temperatures, crystallization is slow and active site formation is insufficient, leading to low oxygen activation and substrate conversion efficiency. Although high temperature can improve crystallinity, uneven crystal size causes some active sites to be buried, and catalytic activity decreases. Comprehensive analysis shows that 150 °C is a suitable synthesis temperature. Figure S8(B) (see Supporting Information of this paper) shows that with the extension of synthesis time, the conversion gradually increases, while the selectivity to p-cymene first increases and then decreases, with a peak at 24 h. XRD results show that when the time is short, crystallinity is low and the number of active sites is limited, so the reaction efficiency is not high. Appropriately extending the synthesis time can form more active sites and improve catalytic activity. However, too long a time will lead to excessive acid sites, which, although beneficial for oxygen activation, may cause side reactions and reduce product selectivity. Therefore, 24 h is a better synthesis time. Figure S9(A) (see Supporting Information of this paper) shows that increasing air flow rate gradually increases conversion, while product selectivity first increases and then decreases. Too low flow rate leads to insufficient oxygen concentration and limited conversion. Although too high flow rate can accelerate the reaction, it may cause excessive surface active oxygen on the catalyst, triggering side reactions and reducing selectivity. Therefore, the optimal air flow rate is 30 mL/min. Figure S9(B) (see Supporting Information of this paper) shows that increasing catalyst dosage can improve conversion and selectivity, but after excessive dosage, conversion tends to be stable and selectivity slightly decreases. With a small amount of catalyst, active sites are insufficient and reaction efficiency is low. Excessive dosage leads to redundant active sites, which has limited improvement on conversion, and too many acid sites will aggravate side reactions. Therefore, the suitable catalyst dosage is 50 mg. In Figure S9(C) (see Supporting Information of this paper), increasing reaction temperature increases conversion, and selectivity first increases and then decreases. At low temperatures,

energy is insufficient and molecular activation is slow; too high temperature promotes side reactions. Comprehensive analysis shows that a better reaction temperature is 30 °C. Figure S9(D) (see Supporting Information of this paper) shows that extending reaction time can increase conversion, but selectivity gradually decreases. The increase in conversion is due to continuous substrate activation and oxygen supply, while the decrease in selectivity may be related to secondary reactions caused by product accumulation. Considering comprehensively, the optimal reaction time is 10 h.

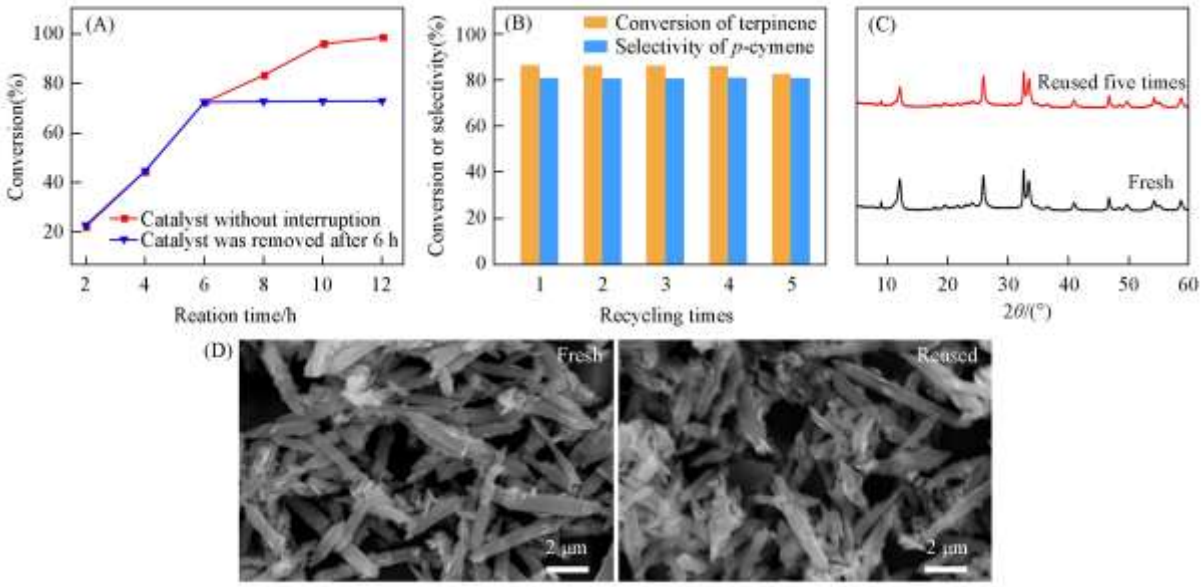

Figure 7 Recycling stability testing and related characterization of catalyst (a) Leaching experiment; (b) recycling experiment; (c) XRD; (d) SEM.

The durability of $Bi_2Fe_2Co_4$-MOF-BDC-150-24 was probed through hot-filtration and consecutive-run assays (Figure 7). As shown in Figure 7A, withdrawal of the solid catalyst at the 6 h mark halted any further substrate turnover despite prolonged reaction time, confirming that the process is truly heterogeneous and that the active species remain firmly anchored to the framework without leaching. Figure 7B demonstrates that over multiple recovery cycles the conversion level stays essentially unchanged, attesting to the robust and stable catalytic behaviour of the $Bi_2Fe_2Co_4$-MOF-BDC-150-24 material. At the same time, the recovered catalyst was characterized and compared with the unused catalyst. The results in Figure 7(C) show that the crystal structure of $Bi_2Fe_2Co_4$-MOF-BDC-150-24 material after 5 uses did not change significantly compared with the unused catalyst. The results in Figure 7(D) prove that the crystal morphology of the catalyst did not change significantly during use. Combined with reaction results and related characterization, $Bi_2Fe_2Co_4$-MOF-BDC-150-24 material has excellent recycling performance.

Table 2 Results of oxidative dehydrogenation of other molecules with similar structure

Entry	Substrate	Product	Conversion(%)	Selectivity(%)
1	Terpinene	p-Cymene	96.1	88.5
2	Phellandrene	p-Cymene	97.2	94.9
3	γ-Terpinene	p-Cymene	93.9	99.9

a. Reaction conditions: 50 mg catalyst, 3 mmol substrate, 10 g cyclopentanone, 30 °C, 10 h, air flowrate: 30 mL/min; b. terpinene; c. phellandrene; d. γ-terpinene; e. p-cymene.

To explore the application potential of the catalyst, the catalytic oxidative dehydrogenation of $Bi_2Fe_2Co_4$-MOF-BDC-150-24 for different terpinene-like molecules was studied, and the data are listed in Table

2. From the data in the table, it can be seen that when two C=C bonds on the ring are in a conjugated state (Entries 1, 2), although the substrate conversion can reach more than 96%, there are a large number of by-products in the obtained products. It can also be observed that the position of conjugated double bonds also has a significant impact on product selectivity. The distribution of conjugated double bonds in the terpinene molecule leads to 4 active α-H sites, while the phellandrene molecule has only 3 similar active sites, so the product selectivity of phellandrene oxidation to p-cymene is higher. As for γ-terpinene molecule (Entry 3), although it also has 4 active α-H sites in its molecule, its two C=C bonds are not in a conjugated state, so the reactivity of α-H sites is significantly reduced, showing high selectivity when oxidized to p-cymene.

4 Conclusion

In this paper, a series of BiFeCo-MOFs materials were successfully prepared under static solvothermal conditions, and their synthesis conditions and the oxidative dehydrogenation reaction parameters of terpinene were systematically optimized, ultimately achieving an efficient aerobic oxidative dehydrogenation of terpinene. The materials were characterized in detail by XRD, IR, FE-SEM, XPS and other means. Among them, the $Bi_2Fe_2Co_4$-MOF-BDC-150-24 material has regular shuttle-shaped crystal morphology while maintaining high crystallinity, and there is electron transfer between Fe^{3+} and Co^{2+}, which is beneficial for the Co^{2+} active sites to dissociate and activate oxygen molecules in air during the oxidative dehydrogenation reaction. NH_3-TPD characterization shows that due to the introduction of Bi^{3+}, multi-metal $Bi_2Fe_2Co_4$-MOF-BDC-150-24 has strong acidity, which is beneficial to the adsorption and activation of substrate molecules, thereby achieving efficient aerobic oxidative dehydrogenation of terpinene. The $Bi_2Fe_2Co_4$-MOF-BDC-150-24 catalyst exhibits excellent catalytic performance in the oxidative dehydrogenation of terpinene, and also shows good catalytic performance and substrate adaptability for other substrates with structures similar to terpinene. In addition, the results of cycling stability tests show that the catalyst has good stability.

References

[1] Xiong C., Chen S., Yang P., Zha S., Zhao Z. J., Gong J., ACS Catalysis, 2019, 9(7), 5816 5827
[2] Fu Z., Li D.Z., Zhou L.D., Li Y.M., Guo J.W., Li Y.Q., Liu H.M., Zhang Q.J., Petroleum Science, 2023, 20(4), 2488 2498
[3] Han R., Diao J.Y., Kumar S., Lyalin A., Taketsugu T., Casillas G., Richardson C., Liu F., Yoon C. W., Liu H.Y., Sun X.D., Huang Z.G., J. Energ. Chem., 2021, 57, 477 484
[4] Wang G.M., Zhang X.F., Yan Y., Appl. Catal.: Gen., 2021, 628, 118402
[5] Lv H.P., Laishram R.D., Yang Y., Li J.Y., Xu D.D., Zhan Y., Luo Y., Su Z.M., More S., Fan B.M., Org. Biomol. Chem., 2020, 18, 3471 3474
[6] Guan J.H., Jiang H.X., Yang G.C., Wang L.T., Gong H., Chem. Eng. J., 2026, 527, 171976
[7] Hu Y., Li X.M., Liu M.Y., Bartling S., Lund H., Rabeah J., Dyson P.J., Beller M., Jagadeesh R. V., ChemCatChem, 2024, 16(1), e202301027
[8] Llopis N., Gisbert P., Baeza A., Correa Campillo J., Adv. Syn. Catal., 2022, 364(6), 1205 1210
[9] Ahn S., Alayoglu S., Notestein J.M., J. Phys. Chem. C, 2024, 128(34), 14305 14314
[10] Wang W.L., Hu S.X., Li L.J., Gao W.L., Cong R.H., Yang T., J. Catal., 2017, 352, 130 141
[11] Doke D.S., Khomane S.B., Pandhare S.L., Dongare M.K., Dumeignil F., Umbarkar S.B., Appl. Catal. A: Gen., 2019, 587, 117246
[12] Gairola P., Millot Y., Krafft J.M., Averseng F., Launay F., Massiani P., Jolivalt C., Reboul J., Catal. Sci. Technol., 2020, 10, 6935 6947
[13] Cruz Navarro J.A., Hernandez Garcia F., Romero G.A.A., Coordin. Chem. Rev., 2020, 412, 213263
[14] Zhao X.X., Li J.Z., Li X., Huo P.W., Shi W.D., Chin. J. Catal., 2021, 42, 872 903
[15] Mu Z.X., Xie P.T., Alshammari A.S., El Bahy S.M., Ren J., Liang G.M., He M.K., El Bahy Z.M., Zhang P., Liu C.Z., Adv. Compos. Hybrid Mater., 2024, 7, 171
[16] Jin H.G., Zhao P.C., Qian Y.Y., Xiao J.D., Chao Z.S., Jiang H.L., Chem. Soc. Rev., 2024, 53, 9378 9418
[17] Dong Y.H., Lu X.H., Yang L., Sun F.Q., Duan J.G., Guo H.T., Zhang Q.J., Zhou D., Xia Q.H., Chem. J. Chinese Universities, 2022, 43(11), 20220458
[18] Liu H., Yi W.W., Li Q.Q., Zhao S.Y., Inorg. Chem. Front., 2024, 11, 5973 5978
[19] Zwolinski K. M., Chmielewski M. J., ACS Appl. Mater. Interfaces, 2017, 9, 33956 33967

[20] Sun F.Q., Guo H.T., Zhang W., Li T., Lu X.H., Zhao L., Zhou D., Xia Q.H., Mol. Catal., 2024, 557, 111958
[21] Xia L., Chen H.P., Wang W.Z., Jia X.G., Zhang D.K., Wang L., Wu P.F., Li L.L., Huang J., J. Mater. Sci. Technol., 2024, 202, 39 49
[22] Zeng T.Q., Sun G., Miao C.X., Yan G., Ye Y.C., Yang W.M., Sautet P., ACS Catal., 2020, 10(21), 12888 12897
[23] Zhang W., Lu X.H., Dong Y.H., Guo H.T., Yan S., Zhou D., Xia Q.H., Chem. J. Chinese Universities, 2025, 46(4), 20240555
[24] Li T., Lu X.H., Li X.X., Cheng R., Guo H.T., Zhan J.H., Zhou D., Xia Q.H., Chem. J. Chinese Universities, 2024, 45(12), 20240367
[25] Chen Q.Q., Yang X.B., Lv Y.C., Pan J.J., Cheng K.J., Inorg. Chem. Commun., 2025, 171, 113617
[26] Li R.B., Chen Z.M., Cai M.X., Huang J.X., Chen P., Liu G.G., Lv W.Y., Appl. Surf. Sci., 2018, 457, 726 734
[27] Guo H.T., Lu X.H., He J., Zhang H.X., Zhang H.F., Dong Y.H., Zhou D., Xia Q.H., Mater. Chem. Phys., 2023, 294, 127001